Contents lists available at ScienceDirect

Fuel

journal homepage: www.elsevier.com/locate/jfue

Full length article

Characteristics of heat release rate spectra in turbulent flames with different fuels

Ankit D. Kumar [a,b,*], Preethi Rajendram Soundararajan [c], Caleb J. Li [a], James C. Massey [a,b], Nedunchezhian Swaminathan [a]

[a] *Department of Engineering, University of Cambridge, Trumpington Street, Cambridge CB2 1PZ, United Kingdom*
[b] *Robinson College, University of Cambridge, Grange Road, Cambridge CB3 9AN, United Kingdom*
[c] *Department of Aeronautics and Astronautics, University of Southampton, Southampton SO16 7QF, United Kingdom*

HIGHLIGHTS

- Global heat release rate spectra in turbulent flames exhibit a −5th power decay.
- Classical −2.5-power scaling appears only in canonical jet-in-cross-flow flames.
- The higher decay rate is due to the faster decay of the correlation volume spectra.
- Local heat release rate spectra are modelled using non-reacting flow velocity.

ARTICLE INFO

Keywords:
Heat release rate spectra
Hydrogen fuel
Liquid spray fuels
Combustion noise

ABSTRACT

Direct combustion noise arises from pressure fluctuations caused by the unsteady heat release rate (HRR) and its spectral content is influenced by the spectral behaviour of HRR, which is investigated in this study. The unsteady HRR is either directly obtained from large eddy simulations (LES) or approximated using OH* chemiluminescence measurements for various flames in three configurations: a lean direct injection hydrogen combustor, a single-injector hydrocarbon-spray burner with swirling air, and a jet-in-cross-flow hydrogen burner. The volume-integrated HRR spectra exhibit a high-frequency scaling of f^{-5} in all the cases except for the jet-in-cross-flow flames. These results are explained using the spectral characteristics of local HRR and its correlation volume. Furthermore, the validity of a model for volume-integrated HRR spectra based on non-reacting flow turbulent kinetic energy spectra is evaluated.

1. Introduction

Aircraft noise negatively impacts frequent flyers and communities near airports, causing long-term hearing damage and sleep disruption [1]. These impacts will become more detrimental as the global air traffic increases [2]. While jet, fan and external aerodynamic noise have reduced in the last few decades, combustion noise remains a major contributor to overall aircraft noise [1,3]. Therefore, further reduction in total aircraft noise requires a closer understanding and accurate modelling of combustion noise.

Direct combustion noise arises from pressure fluctuations caused by unsteady heat release rate (HRR) [4]. The direct noise spectra depend on the local HRR spectrum and the Green's function that relates acoustic fluctuations to HRR fluctuations [5]. If the spatio-temporal variation of the Green's function is negligible then, the noise spectrum is determined solely by the volume-integrated (global) HRR spectrum [4]. This condition is satisfied under the assumptions of a compact flame and far-field acoustics [6]. The global HRR spectrum shows negligible frequency variation below a frequency given by U_b/L, with U_b and L representing the bulk-mean velocity and a typical flame length, respectively [7]. A past theoretical study [8] showed that the HRR spectrum decayed as $f^{-5/2}$ for $f > f_c$. Rajaram and Lieuwen [9] showed that the global HRR spectra of Bunsen flames had a similar decay ($\sim f^{-2.2}$). However, Kumar et al. [10] showed that this HRR spectrum decayed as f^{-5} in swirl-stabilised, bluff body and jet-in-cross-flow (JICF) flames computed using large eddy simulations (LESs). Experimental evidence for this scaling is lacking, and its dependence on flame configuration and fuel remains unclear. This scaling plays a critical role in predicting sound pressure level (SPL) spectra

---

* Corresponding author at: Department of Engineering, University of Cambridge, Trumpington Street, Cambridge CB2 1PZ, United Kingdom.
Email address: adk46@cam.ac.uk (A.D. Kumar).

https://doi.org/10.1016/j.fuel.2026.138409
Received 28 August 2025; Received in revised form 21 November 2025; Accepted 13 January 2026

and past studies showed $f^{-5/2}$ in premixed flames or steeper decay in non-premixed, ranging from $f^{-10/3}$ to f^{-4} [11–13].

Compressible reacting flow LES captures the spectral characteristics of HRR quite well and offers reasonable estimates of SPL when combined with a far-field computational aeroacoustic (CAA) method [14]. Large computational overheads for this combined approach make it unsuitable for parametric evaluations of SPL. Using acoustic network models with LES or Reynolds averaged Navier Stokes (RANS) simulations overcomes these challenges [15–18]. Additionally, low order models (LOM) allow low-cost estimates of SPL [19], but rely on a modelled HRR spectrum, which dictates their accuracy. The HRR spectra are often modelled using Kolmogorov's turbulence spectrum [20]. However, this model has severe limitations as discussed by Kumar et al. [10], who propose an alternative model that is physically motivated, uses fewer parameters and accounts for different spectral decay rates of HRR and velocity spectra.

The f^{-5} decay in global HRR spectra has so far been observed only for gaseous fuels [10], and its applicability to liquid fuels and other flame configurations remains an open question. This is particularly important since aviation engines use liquid fuels. Recent studies on SPL of spray flames in an axially-controlled stoichiometry (ACS) combustor [21] showed the $f^{-2.5}$ decay, whereas a steeper ($\approx f^{-5}$) decay for SPL was observed in a rich-quench-lean (RQL) combustor [22]. Thus, further investigations of HRR spectra in spray flames are needed for SPL prediction. The universality of f^{-5} scaling in HRR allows quick and easy noise estimation when the Green's function spectrum varies negligibly. If the Green's function spectrum varies appreciably with frequency and spatial location, combustion noise depends on the local HRR spectra, which can be modelled using easily obtained non-reacting flow turbulent kinetic energy (TKE) spectrum [10]. However, the model for local HRR spectra requires the HRR variance, which is unknown a priori. Hence, this study aims: (i) to propose a model for the unclosed HRR variance and (ii) to present experimental evidence supporting an f^{-5} decay in the global HRR for a variety of flames.

A theoretical background is presented in the next section. Section 3 outlines the experimental cases analysed, along with a description of the numerical setup and computational methodology. The results are discussed in Section 4 and the conclusions are summarised in Section 5.

2. Background

In low-Mach number turbulent combustion, where the material derivative of pressure is small and the ratio of specific heat capacities depends weakly on temperature, the pressure perturbation generated by HRR fluctuation per unit volume $\dot{q}'$ is given by [5,19]

$$p'(\boldsymbol{x},t) = \int_{-\infty}^{\infty}\int_{V_f} G(\boldsymbol{y},\boldsymbol{x},t-\tau)\times\frac{\partial}{\partial\tau}\left(\dot{q}'(\boldsymbol{y},\tau)\right)\,\mathrm{d}^3\boldsymbol{y}\,\mathrm{d}\tau, \tag{1}$$

where G is the Green's function that quantifies the pressure perturbation at $(\boldsymbol{x},t)$ due to an impulse $\dot{q}' = \delta(\boldsymbol{x}-\boldsymbol{y},t-\tau)$ and τ is the retarded time given by $\tau = r/c_o$ with c_o being the mean speed of sound. The Power Spectral Density (PSD) of pressure fluctuations is derived using the Fourier transform of the two-point correlation of pressure and its complex conjugate yielding

$$\hat{\wp}(\boldsymbol{x},f) = f^2\int_{V_f}\int_{V_f}\overline{\hat{G}(\boldsymbol{y}_a,\boldsymbol{x},f)\hat{G}^*(\boldsymbol{y}_b,\boldsymbol{x},f)}\times\psi_{\dot{q}}(\boldsymbol{y}_a,\boldsymbol{y}_b,f)\,\mathrm{d}^3\boldsymbol{y}_a\,\mathrm{d}^3\boldsymbol{y}_b, \tag{2}$$

where $\psi_{\dot{q}}$ is the PSD of $\dot{q}'$. Since the Green's function spectrum varies negligibly over the combustor volume [19], Eq. (2) can be approximated as

$$\hat{\wp}(\boldsymbol{x},f) \approx f^2\int_{V_f}|\hat{G}(\boldsymbol{y},\boldsymbol{x},f)|^2\cdot\psi_{\dot{q}}(\boldsymbol{y},f)V_{\mathrm{cor}}\,\mathrm{d}^3\boldsymbol{y}, \tag{3}$$

where V_{cor} is the correlation volume for $\dot{q}'$, which is the product of correlation length scales in three spatial directions [7]. A measure of this length scale is obtained using [9]

$$\gamma^2(x,x+\Delta x,f) = \exp\left(-\frac{\Delta x}{l_{\mathrm{cor}}(f)}\right)^2, \tag{4}$$

where Δx is the distance between the maximum HRR location and an arbitrary point x in the flame region. The coherence, γ^2, is

$$\gamma^2(x,x+\Delta x,f) = \frac{|\breve{\psi}_{\dot{q}}(x,x+\Delta x,f)|^2}{\breve{\psi}_{\dot{q}}(x,x,f)\,\breve{\psi}_{\dot{q}}(x+\Delta x,x+\Delta x,f)}, \tag{5}$$

where $\breve{\psi}_{\dot{q}} = \int\int\psi_{\dot{q}}\,\mathrm{d}y\,\mathrm{d}z$. The correlation lengths in the other two directions are obtained similarly. If the Green's function spectrum varies negligibly with frequency and spatial location [19], Eq. (3) indicates that the PSD of pressure fluctuations depends directly on the PSD of the volume-integrated HRR, $\psi_{\dot{Q}}$, rather than the local HRR. Otherwise, the local spectral characteristics of the HRR influence $\hat{\wp}$. This study primarily examines the volume-integrated HRR spectra and also considers the local HRR spectra when they are available.

3. Description of burner configurations, experimental and numerical setup

The operating conditions of the sixteen cases studied are listed in Table 1. Three cases are in the single-nozzle LDI burner (SNB301, SNB402, and SNB405), two from the LDI multi-burner cluster (MBC30 and MBC60), eight from SICCA (S1 to S8) and three from JICF (JICF1 to JICF3). All the cases are operated at atmospheric pressure with various gaseous and liquid fuels as noted in the table.

3.1. Lean direct injection (LDI) burners

Fig. 1(a) shows the schematic of the single-nozzle burner (SNB) from University College London (UCL). The injector comprises a 6.7 mm diameter air nozzle and two 0.9 mm diameter fuel nozzles placed diametrically opposite to each other in a JICF configuration. The central nozzle is surrounded by twelve 1 mm diameter pilot holes that stabilise a stoichiometric H_2–air pilot flame at a bulk mean velocity of 95 m/s. More details on the experimental setup can be found in Ref. [23].

The SNB cases are studied only using LES [24,25] by solving the fully compressible Favre-filtered transport equations for mass, momentum, and total enthalpy. The dynamic Smagorinsky model is used for the eddy viscosity required for the sub-grid residual stress tensor [26,27]. A presumed joint probability density function (PDF) approach with tabulated chemistry [28–30] is used to model the filtered reaction rate. The look-up table is generated using freely propagating laminar premixed flame solutions obtained using the SkeleCHy mechanism [31]. For this approach, the mixture fraction ξ is defined using Bilger's definition [32] and the reaction progress variable is defined as $c = Y_{\mathrm{H_2O}}/Y^{\mathrm{eq}}_{\mathrm{H_2O}}$, with the superscript "eq" representing the equilibrium value for the local mixture fraction. Thermochemical quantities are functions of $\widetilde{\xi}$, $\widetilde{c}$, and their respective sub-grid scale (SGS) variances. These four control variables and the total enthalpy are obtained from their transport equations as described in Refs. [29,30].

Fig. 1(a) shows that the computational domain comprises of an additional domain downstream of the combustion chamber that mimics the pressure far-field conditions in the ambient room. The simulations are performed using OpenFOAM v7 with its PIMPLE algorithm for the pressure-velocity coupling. Second-order central difference and first-order implicit Euler schemes are used for the spatial and temporal derivatives, respectively with a time step of $\Delta t = 50$ ns to ensure numerical stability. The maximum Courant-Friedrichs-Lewy (CFL) number is 0.4 in the whole domain.

Fig. 1(b) shows the schematic of the multi-burner cluster (MBC) which is similar to the single-nozzle counterpart except that the former has 9 air-channels and no pilot flames. In each air channel, hydrogen is injected through two diametrically opposite 0.9 mm nozzles. A photomultiplier with an OH* filter (centred at 310 nm) measures the intensity

Table 1
Operating conditions for the cases studied, where U_b is the bulk mean air velocity, ϕ_g is the global equivalence ratio, l_c is the length of the combustion chamber, f_p are the peak frequencies, f_t is the threshold frequency and S is the swirl number.

Case	Fuel	U_b (m/s)	ϕ_g $(-)$	l_c (mm)	f_p (Hz)	f_t (Hz)	S $(-)$	Results
SNB301	H_2	30	0.12	120	–	1500	–	LES
SNB402	H_2	40	0.2	120	–	1500	–	LES
SNB405	H_2	40	0.5	120	–	700	–	LES
MBC30	H_2	30	0.2	120	128 & 791	791	–	Exp.
MBC60	H_2	60	0.2	120	94 & 820	820	–	Exp.
S1	C_7H_{16}	42.7	0.85	115	322	534	0.60	Exp.
S2	C_7H_{16}	42.7	0.85	165	585	1122	0.60	Exp.
S3	C_3H_8	37.7	0.95	165	383	984	0.70	Exp.
S4	C_7H_{16}	42.7	0.85	165	965	1572	0.70	Exp.
S5	C_7H_{16}	37.7	0.95	165	331	961	0.70	Exp.
S6	$C_{12}H_{26}$	37.7	0.95	165	502	817	0.70	Exp.
S7	C_7H_{16}	42.7	0.85	115	653	1550	0.59	Exp.
S8	C_7H_{16}	42.7	0.85	165	970	1588	0.59	Exp.
JICF1	H_2	3.7	0.044	50	–	≈ 100	–	Exp.
JICF2	H_2	3.7	0.107	50	–	≈ 100	–	Exp.
JICF3	H_2	3.7	0.107	50	–	≈ 120	–	Exp.

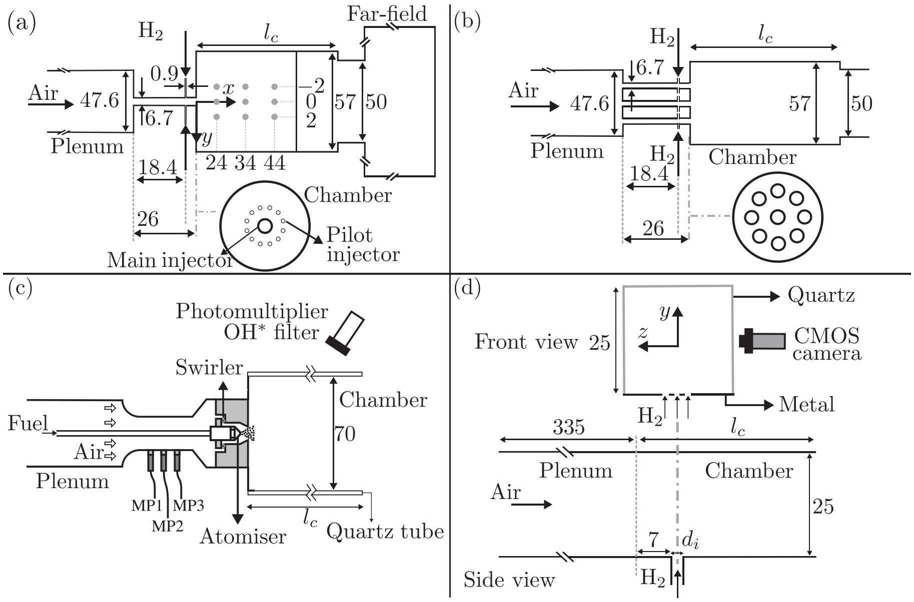

Fig. 1. Schematics of (a) the computational domain for single-nozzle burner, (b) multi-burner cluster, (c) SICCA-spray combustor and (d) JICF combustor. The orientation of the coordinate axes is identical for all configurations. Time-series data for HRR and reacting and non-reacting velocity are extracted from nine probe locations shown using grey coloured markers in (a). All dimensions are in mm.

of OH* chemiluminescence (CL) at an acquisition rate of 10 kHz. Further details of the MBC experimental setup are discussed in Ref. [33].

3.2. SICCA combustor

A schematic of the experimental setup of the single-injector swirl-spray SICCA combustor from the EM2C laboratory is shown in Fig. 1(c). Air enters through the plenum at a mass flow rate of 2.6 g/s and flows into the combustion chamber through a clockwise-oriented six-channel tangential swirler. Three swirlers are used, each with a different swirl number listed in Table 1 [34,35]. When operating with heptane, the fuel enters through a central tube in the plenum and passes through a simplex atomiser which delivers a hollow-cone fuel spray into the combustion chamber. With propane, the fuel and air are fully premixed before entering the plenum. Quartz combustor walls provide optical access, with their lengths for various operating conditions noted in Table 1. The OH* CL intensity is measured using a photomultiplier with an OH* filter (centred at 308 nm) at an acquisition rate of 16.4 kHz. Additional details of this experimental setup can be found in Ref. [35].

3.3. JICF burner

The jet-in-cross-flow burner is shown schematically in Fig. 1(d) [36]. Air passes through a square cross-section plenum with a side length of 25 mm and 335 mm in length. Three sides of the combustion chamber are made of quartz plates which provide optical access, and the fourth side consists of a metal plate that houses the hydrogen injection assembly. This metal plate consists of three injection holes located at a distance of 7 mm from the inlet of the optically accessible chamber with a spacing of 5 mm between the holes. The hydrogen injection plate includes a small settling chamber at its rear to ensure uniform flow rates through all three injection holes.

For case JICF1, fuel is injected at $U_j = 78$ m/s through a single 1 mm port. In JICF2 and JICF3, the fuel is delivered at $U_j = 255$ m/s and $U_j = 64$ m/s through three ports, each with diameters of 0.5 and 1 mm respectively. A CMOS high-speed camera equipped with an optical filter centred at 320 nm is used to capture the OH*. The OH* CL is used here as a reliable marker for HRR, based on recent findings in diffusion hydrogen flames [37]. Discrepancies between OH* and HRR in regions where

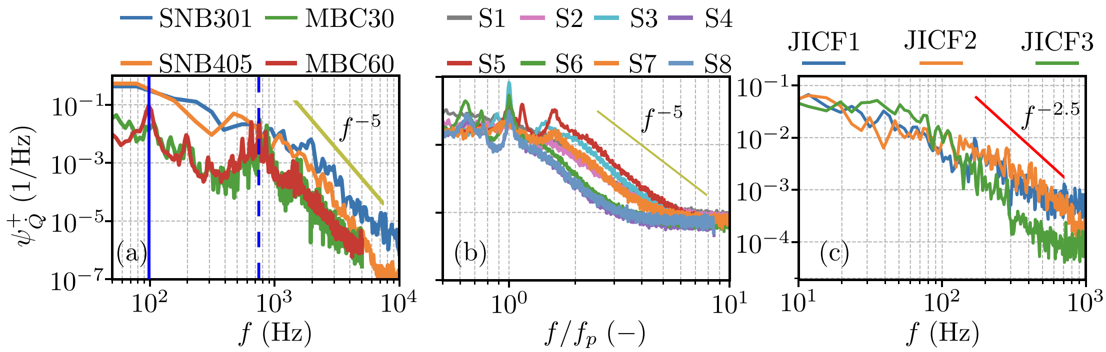

Fig. 2. Normalised volume-integrated HRR (for SNB cases) or OH* intensity (for all other cases) frequency spectra for (a) LDI burners, (b) SICCA-spray combustor and (c) JICF combustor, where $\psi^+_{\dot{Q}}$ is normalised by the variance of the volume-integrated HRR (or OH* intensity) given by $\int_0^\infty \psi_{\dot{Q}}\, \mathrm{d}f$. Solid and dashed blue lines mark the plenum and chamber mode frequencies for case MBC60, respectively. The spectra for the SICCA cases are shown in normalised frequency space, where f_p corresponds to the quarter wave mode frequency in the chamber. (For interpretation of the references to colour in this figure legend, the reader is referred to the web version of this article.)

the flame burns in a rich premixed mode affect time-averaged values [38]. However, these discrepancies are not expected to affect the spectral decay rates of species mass fractions and HRR, which are governed by the turbulence cascade [39]. The camera is operated at 4 kHz with an acquisition time of 1.36 s.

4. Results

This section discusses the volume-integrated HRR spectra, the frequency dependence of its correlation volume and a simple empirical model for local HRR spectra.

4.1. Characteristics of global and local HRR spectra

Fig. 2 presents the volume-integrated (or global) HRR spectra, $\psi^+_{\dot{Q}}$, with the superscript + denoting the spectrum normalised by the HRR variance given by $\int_0^\infty \psi_{\dot{Q}}\, \mathrm{d}f$, for the four configurations discussed in Section 3. The HRR variance is obtained by integrating the HRR PSD over the entire frequency range. Equivalently, it can be computed as the time-average of $\left(\dot{Q}'\right)^2$. The global HRR is deduced from the LES for SNB cases and approximated using OH* CL intensity for the other three configurations. Unlike SNB cases, the MBC cases exhibit multiple narrowband peaks in the global HRR spectra. The two peak frequencies marked in Fig. 2(a) correspond to the plenum and chamber acoustic modes, while the other narrowband peaks arise from quasi-periodic oscillations due to nonlinear interactions between these modes [40]. Fig. 2(b) shows the variation of the normalised global HRR spectra with f/f_p for the SICCA cases, where f_p is the peak frequency corresponding to the quarter-wave chamber mode in each case. Normalising by f_p prevents overlap in the decay region ($f/f_p > 1$), as some cases share similar threshold frequencies (see Table 1). The threshold frequency f_t for the SICCA and JICF cases is defined as the frequency at which $\psi^+_{\dot{Q}}$ falls below 5% of $\psi^+_{\dot{Q}}(f_l)$, where f_l is the reciprocal of the total signal duration. In the MBC cases, f_t is defined by the chamber mode frequency. Since the SNB cases have limited low-frequency resolution, the threshold frequency is determined visually at the onset of the steep spectral decline. Across the SICCA and JICF cases, most of the spectral content remains within one decade for $f/f_p < 1$. Beyond f_t, the spectra decay as $\approx f^{-5}$ for all cases except the JICF case, which decays as $\approx f^{-2.5}$.

The slopes, standard deviations and corresponding frequency intervals of the linear fits to the high-frequency spectra are shown in Fig. 3 for the cases presented in Fig. 2. The lower bound of the frequency interval is given by f_t. The upper bound of the frequency interval in LES is determined by the Nyquist criterion. In the experiments, this upper bound is chosen as the frequency at which the spectra plateau as the signal strength approaches the noise level. It can be seen that apart from the JICF case, the spectral decay slopes for most cases are close to −5. In cases other than JICF, the largest deviations from the −5 slope occur for cases with limited data length (SNB cases), quasi-periodic thermoacoustic oscillations (MBC cases) and cases where the frequency interval is narrow (S1 and S2).

The normalised volume-integrated HRR and filtered OH* mass fraction spectra are compared in Fig. 4 for case SNB405. The filtered OH* mass fraction is obtained directly from the look-up table, which is constructed using the first moment of OH* mass fraction obtained from freely propagating one-dimensional laminar premixed flames. It is observed that both spectra decay as f^{-5} despite some small differences. This result suggests that OH* CL serves as a reliable HRR marker in partially premixed hydrogen flames, at least for the spectral information. The spectral decay rate of reactive scalars is governed by the underlying energy cascade, which depends on the relative chemical and turbulence time scales[41]. Therefore, even though there may be large scale spatial discrepancies in different reactive scalars, their spectral decay rates are expected to be similar [39]. For spray flames, the OH* CL signal can be considered to be a reasonable marker for HRR if they are premixed. It was previously reported that these flames have low levels of equivalence ratio fluctuations, measured using the relative intensity deviation between OH* and CH* [35,42]. Furthermore, the fluctuations of HRR and OH* CL signal are proportional to each other with the quantitative discrepancies arising only at low-frequencies [43]. Therefore, past studies have used fluctuations in OH* CL signal as a reliable marker for HRR fluctuations [9,44–46], even though the spatial distribution of their mean values may not necessarily be identical.

The two different spectral decay rates can be explained using the relationship between global and local HRR spectra given by [10,47]

$$\frac{\psi^+_{\dot{Q}}}{V_F^2} \simeq \begin{cases} \psi^+_{\dot{q}} \big| \ \mathcal{O}\left(V_{\mathrm{cor}}\right) \sim \mathcal{O}\left(V_F\right) \\ \\ 8\psi^+_{\dot{q}} \dfrac{V_{\mathrm{cor}}(f)}{V_F} + \mathcal{O}\left(\dfrac{V_{\mathrm{cor}}(f)}{V_F}\right)^2 \\ \qquad \big| \ \mathcal{O}\left(V_{\mathrm{cor}}\right) \ll \mathcal{O}\left(V_F\right), \end{cases} \tag{6}$$

where V_{cor} is the correlation volume and $V_F = l_x l_y l_z$, where l_x is the distance between the fuel injection point and the axial locations where either $\int\int \bar{\dot{q}}\, \mathrm{d}y\mathrm{d}z$ or $\int\int \overline{\mathrm{OH}^*}\, \mathrm{d}y\mathrm{d}z$ crosses an arbitrarily chosen threshold of 25% of the maximum value [9]. The length scales l_y and l_z are defined in a similar manner. Spectral characteristics of the local HRR are first discussed, followed by the correlation volume spectra.

The analysis in the following discussions is limited to JICF and SNB cases due to the unavailability of spatially resolved data for other cases. Furthermore, since the other cases follow f^{-5} scaling for global HRR

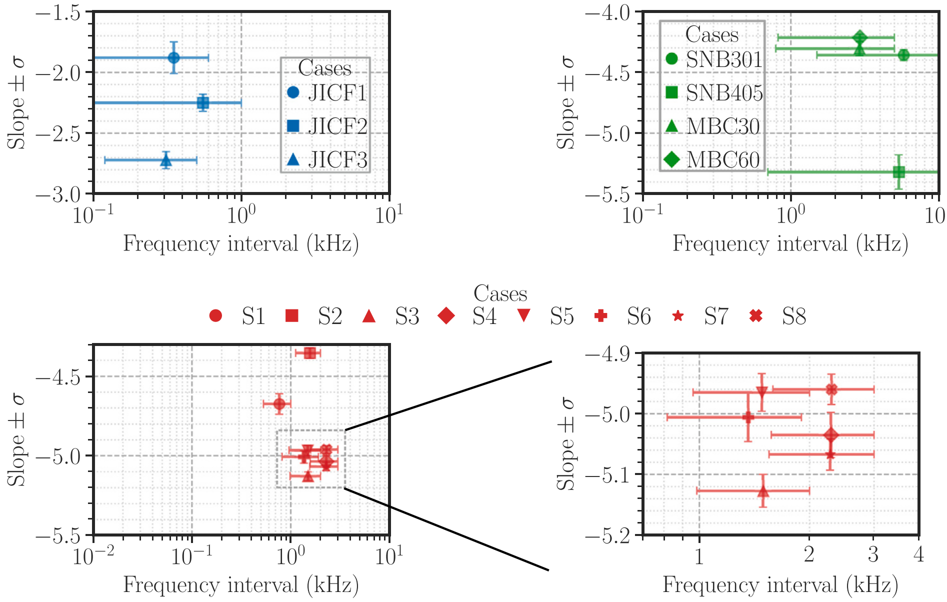

Fig. 3. Scatter plots of spectral decay slopes obtained from linear fits against the frequency interval in which the fit was obtained for all cases shown in Fig. 2. Horizontal and vertical error bars represent the frequency interval and the standard deviation (σ), respectively. The coefficients of determination for each case is > 0.95.

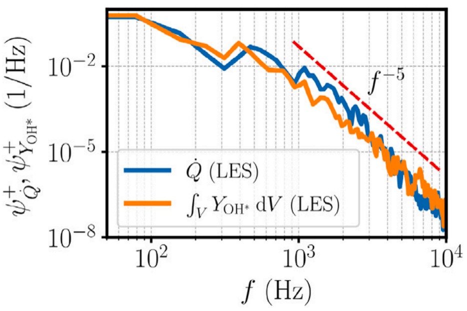

Fig. 4. Normalised volume-integrated HRR and OH* mass fraction (Y_{OH^*}) frequency spectra for case SNB405.

(or OH*), they are expected to behave similarly to SNB cases. Fig. 5(a) shows the normalised time-averaged line-of-sight (LOS) integrated OH* CL contours for JICF2. The PSD of OH* CL signals obtained from three probe locations are shown in Figs. 5(c). The spectral content near the jet exit (probe 1) and flame tip (probe 3) is weak, with decay rates varying as $\leq f^{-1}$. Two peaks appear in the HRR spectra at probe 2, with the spectra decaying as $f^{-2.5}$ beyond the second peak. These peaks are close to the quarter-wave (232.3 Hz) and three-quarter-wave (695.2 Hz) resonance frequencies of the channel [48], computed using OSCILOS, an open-source solver for thermoacoustic eigenvalue problems [49]. The spectral decay at all probe locations in the JICF case follows approximately f^{-2}. Figs. 5(b) and 5d show the normalised $\overline{\dot{q}}$ contours and the PSD of local HRR ($\psi^+_{\dot{q}}$) at three probe locations respectively for SNB405. Unlike the JICF case, $\psi^+_{\dot{q}}$ spectra show the same f^{-2} scaling for all probe locations and no dominant peaks.

The frequency variation of the correlation volume and the respective correlation lengths (L_x, L_y and L_z) for cases SNB405 and JICF2 are shown in Figs. 6(a) and 6b, respectively. The JICF2 case exhibits a slower decay compared to the SNB405 case, which follows a f^{-3} decay similar to the partially premixed cases in [10]. The local HRR and V_{cor} spectra decay as f^{-2} and f^{-3}, respectively, explaining the f^{-5} decay in the global HRR spectra, as described by Eq. (6). The frequency variation of $\overline{\psi^+_{\dot{Q}}} \times V_{\mathrm{cor}}$ shown in Fig. 7 further confirms that the local HRR spectra and V_{cor} spectra result in the f^{-5} decay. This is shown only for SNB405 as a representative case. However, based on previous studies, cases exhibiting a f^{-3} decay in the V_{cor} spectra are expected to show a f^{-5} decay in HRR [10,47]. The converse, that f^{-5} decay in HRR arises due to f^{-3} decay in correlation volume, may not necessarily hold, especially in cases with spatially varying decay rates in HRR spectra [10]. Nevertheless, since the f^{-3} decay in correlation volume arises from large Reynolds numbers or spatial inhomogeneities [10], the converse may also hold for the SICCA cases and potentially for the MBC cases, which share similarities with the SNB cases. Further measurements and analyses are required to confirm this.

The different decay in the correlation volume spectra for cases SNB405 and JICF2 can be explained by the spatial coherence of HRR. Consider the transversely integrated HRR signals, $\int\int \dot{q}'\,\mathrm{d}y\,\mathrm{d}z$, evaluated at the maximum HRR location and at another point separated by a streamwise distance Δx. The argument (angle) of the complex cross-spectrum between these two signals, referred to as the cross-spectrum phase (CSP or $\varphi_{\dot{q}}$), indicates the spatial coherence of the above HRR. Figs. 8(a) and 8d show the frequency variation of CSP for different Δx in cases SNB405 and JICF2, respectively. Unlike the SNB405 case, the CSP in the JICF2 case increases progressively with streamwise distance, reflecting convective effects [9]. Fig. 8(b, e) and (c, f) show the frequency variation of CSP along the y- and z-directions, respectively. In SNB405, CSP exceeds $\pi/2$ in all directions at high frequencies (> 3000 Hz), whereas in JICF2, it exceeds $\pi/2$ only along the streamwise direction. However, the HRR signals contributing to CSP values above $\pi/2$ in JICF2 are very weak. Consequently, the HRR signals are in-phase (CSP $\leq \pi/2$) and strongly correlated across the entire JICF2 flame brush at all frequencies, producing slowly decaying correlation volume spectra. In contrast, the faster decay of the correlation volume spectra in case SNB405 is due to the out-of-phase (CSP $\geq \pi/2$) HRR signals at high frequencies in every direction.

4.2. Modelling aspects

When the Green's function spectrum varies significantly with spatial location or frequency, the local HRR spectra are required for evaluating the PSD of pressure fluctuations, as per Eq. (3). Kumar et al. [10]

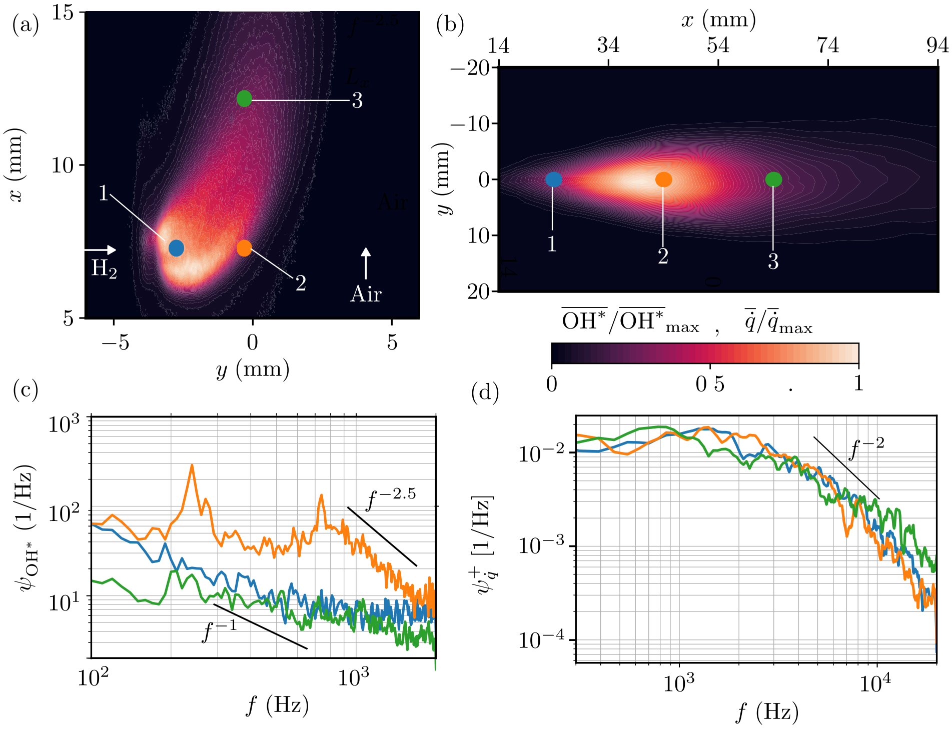

Fig. 5. The normalised time-averaged OH* and its local spectra are shown in (a) and (c) for JICF2 flame. The spatial distribution of time-averaged $\dot q$ and its local normalised spectra obtained from LES are shown in (b) and (d) for case SNB405.

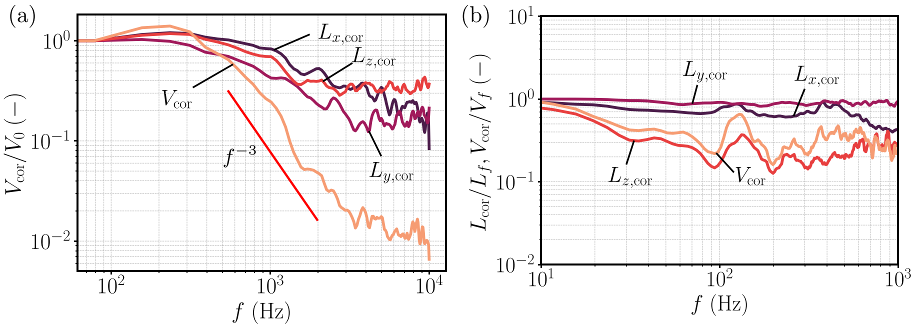

Fig. 6. Correlation length and volume spectra for cases (a) SNB405 and (b) JICF2.

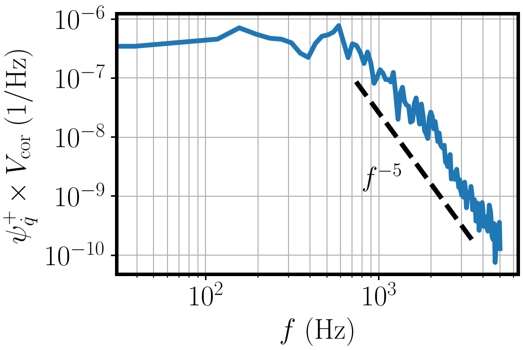

Fig. 7. Frequency variation of the product between $\psi^+_{\dot q}$ and V_{cor} for case SNB405.

proposed $\Psi^+_{\dot q} \approx \Psi^+_{|\boldsymbol{u}|}\left(1+(f/f^*)^l\right)^{1/2}$, where $\Psi^+_{\dot q}$ is the modelled geometric mean of the normalised local HRR spectrum, $\Psi^+_{|\boldsymbol{u}|}$ is the normalised geometric mean of turbulent kinetic energy obtained from different spatial locations, f^* is a characteristic frequency and l is a scaling exponent. Here, this model is tested using LES results for the SNB402 flame. The unnormalised spectrum, $\Psi_{\dot q}$, requires the variance of $\dot q'$ which can be related to the square of the time-averaged HRR following [44]. Hence, the local HRR spectrum is given by

$$\Psi_{\dot q} \approx \left(\mathcal{B}\bar{\dot q}\right)^2 \Psi^+_{|\boldsymbol{u}|}\left(1+\left(\frac{f}{f^*}\right)^l\right)^{1/2}, \qquad (7)$$

where $f^* = 2000$ Hz is defined similarly to f_t and the scaling exponent is chosen as $l = 2$. The reaction intensity, $\mathcal{B}$, is estimated as the slope of the linear regression between rms and time-averaged local HRR from the x-y midplane as shown in Fig. 9(a). For case SNB405, this slope is $\mathcal{B} = 1.31$ with a high correlation coefficient, $R^2 = 0.96$. Fig. 9(b) compares the model in Eq. (7) to the geometric mean of the local HRR spectrum obtained from nine LES probe locations marked in Fig. 1(a). The model, constructed using $\Psi^+_{|\boldsymbol{u}|}$ from reacting and non-reacting LES, compares well with $\Psi_{\dot q}$. The scaling exponent matches those cases in [10] with neither thermoacoustic instabilities nor spatially varying local HRR spectrum. A higher exponent ($l = 3$) would reduce the discrepancy between LES and model spectral decay rates but is avoided to ensure robust

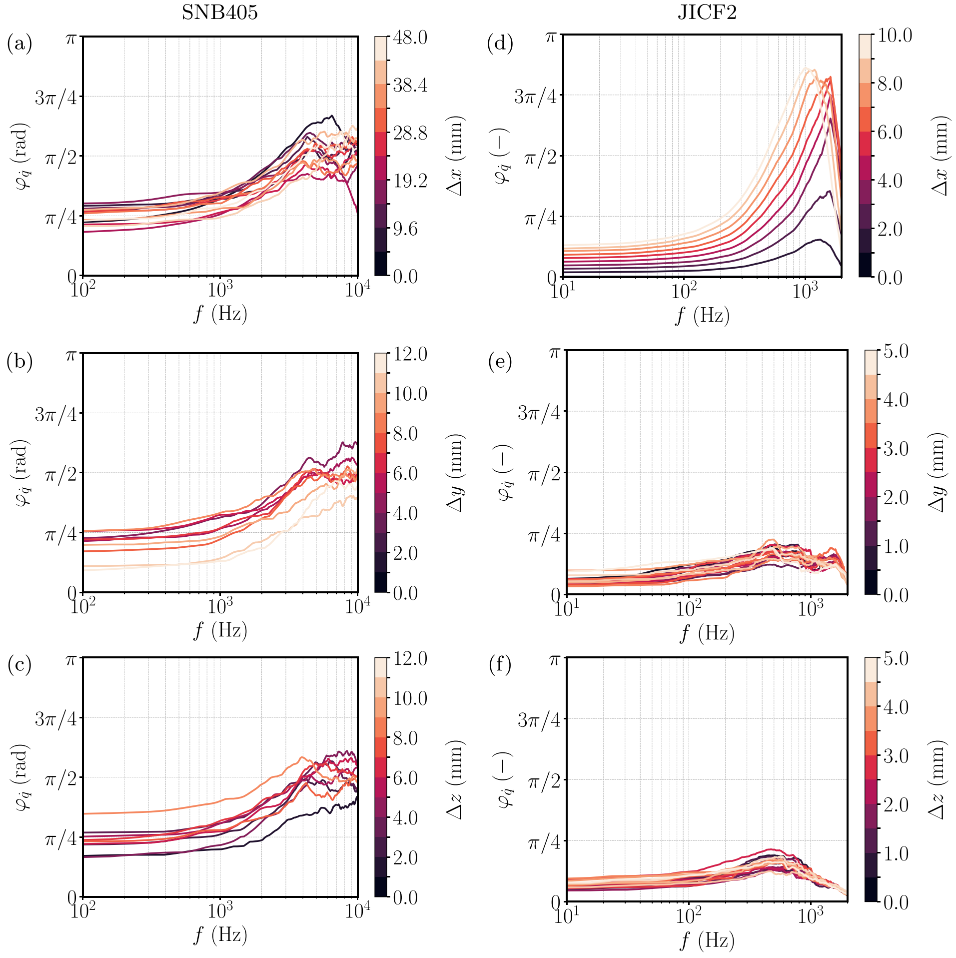

Fig. 8. Frequency variation of the cross-spectrum phase $\varphi_{\dot{q}}$ (Eq. 4) of spatially integrated HRR (OH* CL for JICF2) for cases SNB405 (a–c) and JICF (d–f), respectively. The spatial integrations are performed along y, z (a,d), x, z (b,e), and x, y (c,f) and different coloured lines represent different separation distances used while computing the cross-spectrum.

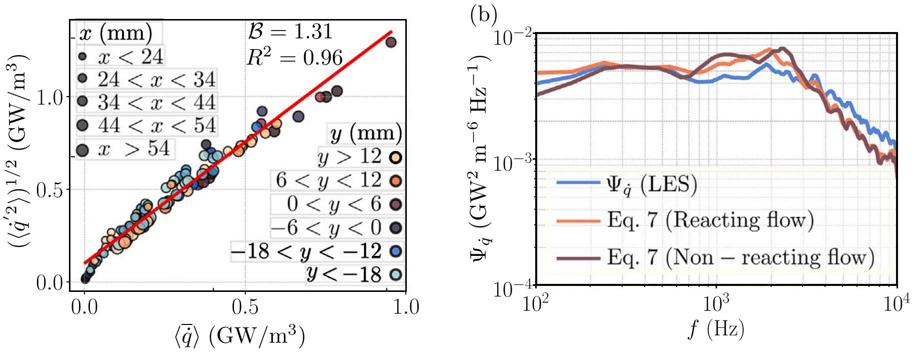

Fig. 9. (a) Correlation between rms and time-averaged HRR obtained from the x-y midplane of SNB405, with marker size and color indicating x and y locations and (b) geometric mean of local HRR spectra from 9 LES probe locations and model spectra from Eq. (7), constructed using LES-based reacting and non-reacting velocity spectra. (For interpretation of the references to colour in this figure legend, the reader is referred to the web version of this article.)

model parameters. The time-averaged HRR, $\overline{\dot{q}}$, can be readily obtained from Reynolds-averaged Navier–Stokes (RANS) simulations [19,44].

Fig. 10 shows instantaneous filtered HRR contours normalised by their maximum for cases SNB301, SNB402, and SNB405. Despite different flame shapes, sizes and structures, these cases have almost the same value for $\mathcal{B}$ although SNB301 has about 8% lower which is because of lower turbulence. SNB301 has a lower reaction intensity ($\mathcal{B} = 1.21$) due to its lower turbulence intensity, which scales with air flow velocity. Additional single- and triple-jet JICF cases spanning two air flow rates, four fuel flow rates per jet and three fuel-port diameters are also considered. In the single-jet cases only the central nozzle of the three-jet cases is present. The reaction intensities for each of the additional cases are shown in Fig. 11 suggesting that $\mathcal{B}$ values are roughly constant for each single-jet case with increasing fuel or air flow rates, but decrease with increasing fuel-port diameter. This sensitivity arises because the fuel-jet velocity scales with the square of the inlet diameter, while it increases

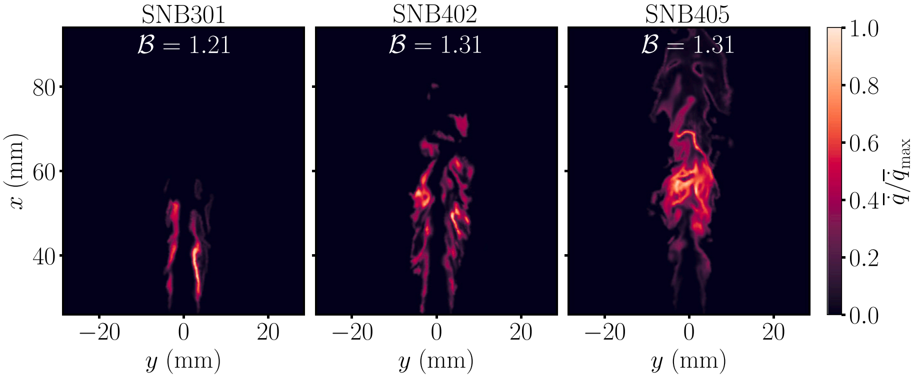

Fig. 10. Contours plots of instantaneous normalised filtered HRR $\overline{\dot{q}}/\overline{\dot{q}}_{\max}$ at arbitrary instants for the SNB cases.

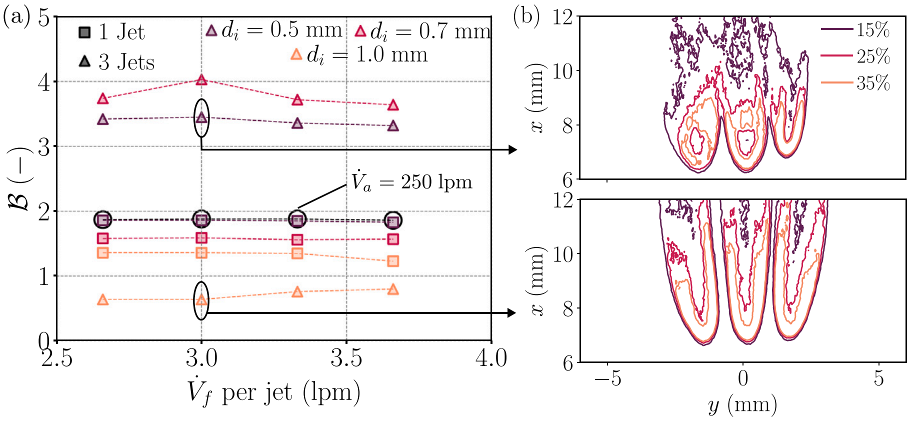

Fig. 11. (a) Variation of reaction intensity $\mathcal{B}$ with fuel flow rate ($\dot{V}_f$) for different JICF cases. Filled and hollow markers correspond to air flow rates ($\dot{V}_a$) of 200 and 250 lpm respectively. (b) Contours of 15%, 25% and 35% $\mathrm{OH}^*_{\max}$ at arbitrary instants for the marked cases.

only linearly with the fuel flow rate. In the triple-jet case, reaction intensity is highest for $d_i = 0.7$ mm. Cases with more pronounced flame surface wrinkling exhibit higher $\mathcal{B}$ values, as shown by OH* contours in Fig. 11(b). The lowest value of $\mathcal{B}$ is for $d_i = 1$ mm, corresponding to the lowest turbulence intensity due to the reduced jet velocity. Notably, triple-jet cases show lower reaction intensity than single-jet cases only at $d_i = 1$ mm. For the triple-jet cases, this may result from reduced turbulence caused by suppressed entrainment, enhanced flame-induced dilatation or destructive interference between coherent structures in the jet interaction regions. The most dominant cause may be deduced using velocity measurements, which will be explored in a future study.

5. Conclusions

The spectral characteristics of global and local HRR for different fuels are analysed in LDI, JICF, and swirl-stabilised flames. Practically relevant cases in an LDI and a swirl-stabilised spray combustor, exhibit a universal f^{-5} decay in global HRR spectra, resulting from the f^{-3} decay of the frequency-dependent correlation volume, V_{cor}. In JICF, where HRR fluctuations remain coherent throughout the flame, V_{cor} decays slowly, leading to a lower decay rate of $f^{-2.5}$.

When the Green's function spectrum varies negligibly (within one decade) across frequency and spatial location, the universality of global HRR spectra enables SPL estimation using empirical models instead of expensive reacting flow simulations or experiments. Otherwise, the noise spectrum depends on the local HRR spectrum, which differs from the global spectra. A previously proposed model for the local HRR spectrum based on the non-reacting flow velocity spectrum is validated for the single-nozzle burner. Moreover, directions for closing the unknown HRR variance term are provided. This model offers a cost-effective approach to deduce HRR spectral information using non-reacting LES and reacting RANS simulations.

CRediT authorship contribution statement

Ankit D. Kumar: Writing – review & editing, Writing – original draft, Visualization, Validation, Software, Methodology, Investigation, Formal analysis, Data curation, Conceptualization. **Preethi Rajendram Soundararajan:** Writing – review & editing, Validation, Investigation, Formal analysis, Data curation. **Caleb J. Li:** Writing – review & editing, Validation, Software, Methodology, Data curation. **James C. Massey:** Writing – review & editing, Validation, Software, Methodology. **Nedunchezhian Swaminathan:** Writing – review & editing, Supervision, Resources, Project administration, Funding acquisition, Conceptualization.

Declaration of competing interest

The authors declare the following financial interests/personal relationships that may be considered as potential competing interests:

Ankit Dilip Kumar reports that financial support was provided by the Cambridge Philosophical Society. Preethi Rajendram Soundararajan reports that financial support, article publishing charges, and travel were provided by the European Union. Caleb J. Li, James C. Massey and Nedunchezhian Swaminathan report that financial support and travel were provided by Mitsubishi Heavy Industries Ltd. If there are other authors, they declare that they have no known competing financial interests or personal relationships that could have appeared to influence the work reported in this paper.

Acknowledgement

A.D.K. acknowledges financial support from the Cambridge Philosophical Society through a Henslow Junior Research Fellowship at Robinson College, University of Cambridge. P.R.S is also thankful to the European Union's Horizon 2020 research and innovation programme Annulight, with grant agreement no. 765998 which enabled the acquisition of the experimental data in SICCA. P.R.S acknowledges the funding received from the Horizon Europe Research and Innovation Programme HESTIA under grant agreement no. 101056865. C.J.L, J.C.M and N.S. acknowledge the financial support from Mitsubishi Heavy Industries, Ltd., Takasago, Japan. This work used the ARCHER2 UK National Supercomputing Service (http://www.archer2.ac.uk). The authors are grateful to ARCHER2 for the financial and computational allocation as a part of an ARCHER2 Pioneer Project (e808). The authors are grateful to Dr. Midhat Talibi and Prof. Ramanarayanan Balachandran for sharing the MBC experimental data. The authors are thankful to Dr. Daniel Durox, Dr. Antoine Renaud, and Prof. Sébastien Candel, EM2C laboratory, France for sharing the SICCA experimental data. P.R.S thanks Prof. E. Mastorakos, University of Cambridge for their contribution to JICF experiments. The authors also thank Christoph Schumann for providing the SkeleCHy mechanism.

Data availability

Data will be made available on request.

References

[1] Dowling AP, Mahmoudi Y. Combustion noise. Proc Combust Inst 2015;35:65–100.

[2] International Air Transport Association (IATA). Global outlook for air transport: deep change. 2024. https://www.iata.org/en/iata-repository/publications/economic-reports/global-outlook-for-air-transport-june-2024-report/.

[3] Ihme M. Combustion and engine-core noise. Annu Rev Fluid Mech 2017;49:277–310.

[4] Strahle WC. A review of combustion generated noise. In: AIAA Aero-Acoustics conf. AIAA; 1973. https://doi.org/10.2514/6.1973-1023

[5] Crighton DG, Dowling AP, Williams JEF, Heckl M, Leppington FG. Thermoacoustic sources and instabilities. In: Modern methods in analytical acoustics: lecture notes. Springer; 1992. pp. 387–405.

[6] Ha S, Lieuwen T. Direct combustion noise: nearfield and non-compactness influences on pressure–heat release coherence. Combust Flame 2025;271:113811.

[7] Wäsle J, Winkler A, Sattelmayer T. Spatial coherence of the heat release fluctuations in turbulent jet and swirl flames. Flow Turbul Combust 2005;75:29–50.

[8] Clavin P, Siggia ED. Turbulent premixed flames and sound generation. Combust Sci Technol 1991;78:147–55.

[9] Rajaram R, Lieuwen T. Acoustic radiation from turbulent premixed flames. J Fluid Mech 2009;637:357–85.

[10] Kumar AD, Massey JC, Murugavel AB, Chen ZX, Swaminathan N. Spectral characteristics of the heat release rate in confined turbulent flames. J Fluid Mech 2025;1007:A29.

[11] Klein SA, Kok JBW. Sound generation by turbulent non-premixed flames. Combust Sci Technol 1999;149:267–95.

[12] Ihme M, Bodony D, Pitsch H. Prediction of combustion-generated noise in non-premixed turbulent jet flames using LES. In: 12th AIAA/CEAS Aeroacoustics Conf 27th AIAA Aeroacoustics Conf; 2006; 2006-2614. pp. 1–16.

[13] Singh KK, Zhang C, Gore JP, Mongeau L, Frankel SH. An experimental study of partially premixed flame sound. Proc Combust Inst 2005;30:1707–15.

[14] Silva CF, Leyko M, Nicoud F, Moreau S. Assessment of combustion noise in a premixed swirled combustor via Large-Eddy simulation. Comput Fluids 2013;78:1–9.

[15] Silva CF, Merk M, Komarek T, Polifke W. The contribution of intrinsic thermoacoustic feedback to combustion noise and resonances of a confined turbulent premixed flame. Combust Flame 2017;182:269–78.

[16] Merk M, Polifke W, Gaudron R, Gatti M, Mirat C, Schuller T. Measurement and simulation of combustion noise and dynamics of a confined swirl flame. AIAA J 2018;56:1930–42.

[17] Merk M, Gaudron R, Silva C, Gatti M, Mirat C, Schuller T, Polifke W. Prediction of combustion noise of an enclosed flame by simultaneous identification of noise source and flame dynamics. Proc Combust Inst 2019;37:5263–70.

[18] Ullrich WC, Mahmoudi Y, Lackhove K, Fischer A, Hirsch C, Sattelmayer T, Dowling AP, Swaminathan N, Sadiki A, Staufer M. Prediction of combustion noise in a model combustor using a network model and a LNSE approach. J Eng Gas Turbines Power 2018;140.

[19] Liu Y, Dowling AP, Swaminathan N, Morvant R, Macquisten MA, Caracciolo LF. Prediction of combustion noise for an aeroengine combustor. J Propuls Power 2014;30:114–22.

[20] Hirsch C, Wäsle J, Winkler A, Sattelmayer T. A spectral model for the sound pressure from turbulent premixed combustion. Proc Combust Inst 2007;31 I:1435–41.

[21] Brouzet D, Krisna B, McCormick D, Reimann CA, Mendoza J, Ihme M. Analysis of direct and indirect noise in a next-generation aviation gas turbine combustor. Combust Flame 2024;260:113249.

[22] Kastenberg LM, Panchal A, Menon S. Direct and indirect combustion noise prediction in a rich-quench-lean combustor using a large eddy simulation. In: AIAA SciTech 2025 forum; 2025. p. 2489.

[23] Dere R, Ezenwajiaku C, Balachandran R, Talibi M. Flame characteristics of a piloted single-nozzle hydrogen lean direct injection (LDI) burner. In: Turbo expo: power for land, sea, and AIR, vol. 87936. ASME; 2024, p. V002T03A016.

[24] Li CJ, Schumann CDK, Dere R, Massey JC, Ezenwajiaku C, Rocha N, Talibi M, Balachandran R, Tanaka Y, Swaminathan N. Influences of momentum flux ratio and fuel injection on flame stabilisation in a lean direct injection burner. Proc Combust Inst 2025;41:105956.

[25] Li CJ, Dere R, Massey JC, Ezenwajiaku C, Schumann CDK, Talibi M, Balachandran R, Tanaka Y, Swaminathan N. Hydrogen lean flame blow-off phenomena in lean direct injection burners. Int J Hydrogen Energy 2025;under review.

[26] Germano M, Piomelli U, Moin P, Cabot WH. A dynamic subgrid-scale eddy viscosity model. Phys Fluids 1991;3:1760–5.

[27] Lilly DK. A proposed modification of the germano subgrid-scale closure method. Phys Fluids 1992;4:633–5.

[28] Ruan S, Swaminathan N, Darbyshire O. Modelling of turbulent lifted jet flames using flamelets: a priori assessment and a posteriori validation. Combust Theory Model 2014;18:295–329.

[29] Chen Z, Ruan S, Swaminathan N. Large eddy simulation of flame edge evolution in a spark-ignited methane-air jet. Proc Combust Inst 2017;36:1645–52.

[30] Massey JC, Chen ZX, Stöhr M, Meier W, Swaminathan N. On the blow-off correlation for swirl-stabilised flames with a precessing vortex core. Combust Flame 2022;239:111741.

[31] Schumann CDK, Cazères Q, Massey JC, Li CJ, Tanaka Y, Swaminathan N. SkeleCHy: a skeletal mechanism for low hydrocarbon content blends with hydrogen. Combust Flame 2025;275:114036.

[32] Bilger RW. The structure of turbulent nonpremixed flames. Proc Combust Inst 1988;22:475–88.

[33] Ezenwajiaku C, Balachandran R, Ducci A, Picciani M, Talibi M. Experimental characterisation of the dynamics of partially premixed hydrogen flames in a lean direct injection (LDI) combustor. In: Turbo expo: power for land, sea, and AIR, vol. 86953. ASME; 2023, p. V03AT04A073.

[34] Vignat G, Durox D, Prieur K, Candel S. An experimental study into the effect of injector pressure loss on self-sustained combustion instabilities in a swirled spray burner. Proc Combust Inst 2019;37:5205–13.

[35] Rajendram Soundararajan P, Durox D, Renaud A, Vignat G, Candel S. Swirler effects on combustion instabilities analyzed with measured FDFs, injector impedances and damping rates. Combust Flame 2022;238:111947.

[36] Rajendram Soundatrarajan P, Gauthier Q, Benie PJ, Mastorakos E. A joint experimental and numerical study of multiple hydrogen flames in a jet in crossflow configuration. Proc Combust Inst 2025;41:105929.

[37] Schiavone FG, Aniello A, Riber E, Schuller T, Laera D. On the adequacy of OH* as a heat release marker for hydrogen–air flames. Proc Combust Inst 2024;40:105248.

[38] Kruljevic B, Darabiha N, Durox D, Vaysse N, Renaud A, Vicquelin R, Fiorina B. Experimentation and simulation of a swirled burner featuring cross-flow hydrogen injection with a focus on the OH* chemiluminescence. Combust Flame 2025;273:113945.

[39] Kolla H, Hawkes ER, Kerstein AR, Swaminathan N, Chen JH. On velocity and reactive scalar spectra in turbulent premixed flames. J Fluid Mech 2014;754:456–87.

[40] Kumar AD, Ezenwajiaku C, Balachandran R, Ducci A, Talibi M, Massey JC, Swaminathan N. Dynamical systems characterization and reduced order modeling of thermoacoustics in a lean direct injection hydrogen combustor. J Eng Gas Turbines Power 2024;146:121008.

[41] Swaminathan N, Chakraborty N. Scalar fluctuation and its dissipation in turbulent reacting flows. Phys Fluids 2021;33.

[42] Rajendram Soundararajan P, Durox D, Renaud A, Candel S. Impact of spray dynamics on combustion instabilities investigated by changing the atomizer recess in a swirl combustor. Combust Flame 2023;252:112757.

[43] Shreekrishna, Acharya V, Lieuwen T. Flame response to equivalence ratio fluctuations—relationship between chemiluminescence and heat release. Int J Spray Combust Dyn 2013;5:329–58.

[44] Swaminathan N, Xu G, Dowling AP, Balachandran R. Heat release rate correlation and combustion noise in premixed flames. J Fluid Mech 2011;681:80–115.

[45] Ha S, Dhanasekaran J, Bapat A, Acuna A, Patel S, Jo S, Wu D, Emerson B, Steinberg A, Lieuwen T. Experimental investigation of broadband noise sources in a swirl stabilized RQL combustor. In: Turbo expo: power for land, sea, and AIR, vol. 86953. American Society of Mechanical Engineers; 2023, p. V03AT04A049.

[46] Lee JG, Santavicca D. Experimental diagnostics for the study of combustion instabilities in lean premixed combustors. J Propuls Power 2003;19:735–50.

[47] Lieuwen TC. Unsteady combustor Physics. Cambridge University Press; 2012.

[48] Rajendram Soundararajan P, Sampath R, Mastorakos E. A combined longitudinal-transverse combustion instability in a hydrogen jet in crossflow configuration. In: Proceedings of the symposium on thermoacoustics in combustion: industry meets academia (2025); 2025. Paper No. 48.

[49] Li J, Morgans AS. Time domain simulations of nonlinear thermoacoustic behaviour in a simple combustor using a wave-based approach. J Sound Vib 2015;346:345–60.